A microplate screen for metal-binding activity based on a nickel-binding protein from *Clostridium carboxidivorans*

Patrick Diep[1], Radhakrishnan Mahadevan[1,2] and Alexander F. Yakunin[1,3]

[1] BioZone Centre for Applied Bioscience and Bioengineering, Department of Chemical Engineering and Applied Chemistry, University of Toronto, Toronto, Ontario, Canada
[2] Institute of Biomaterials and Biomedical Engineering, University of Toronto, Toronto, Ontario, Canada
[3] Centre for Environmental Biotechnology, School of Natural Sciences, Bangor University, Bangor, United Kingdom

Highlights

- purified *Cc*SBPII using an IMAC-aEX protocol with reduced metal contamination and affinity tag removal, validated with ICP-MS, MALDI-ToF and CD
- developed a multiplexed fluorescence assay to characterize binding affinity profile of *Cc*SBPII
- *Cc*SBPII binds to Ni^{2+} at low micromolar affinity, which is strengthened by an order of magnitude in the presence of L-histidine

Abstract

Metal ion specificity of the solute binding protein (SBP) component of ATP-binding cassette (ABC) transporters is determined through binding studies. *Clostridium carboxidivorans* P7T possesses an operon that encodes for an ABC transporter with two SBPs (*Cc*SBPI and *Cc*SBPII) of unknown specificity. Bioinformatics analysis of the operon reveals that the ABC transporter may have a potential role in nickel acquisition based on sequence similarity between the two SBPs and the previously characterized NikZ from *Campylobacter jejuni*. To screen for the uncharacterized ABC transporter's substrate specificity, *Cc*SBPII was purified with minimal metal contamination and affinity tag removal. A ligand titration assay in microplate format was then developed and optimized to detect metal-binding activity using intrinsic protein fluorescence quenching. *Cc*SBPII was found to bind $Cu^{2+} > Ni^{2+} > Co^{2+}$ (K_d 12.2, 32.6, and 142.6 µM, respectively). However, the presence of L-histidine greatly increased *Cc*SBPII affinity to Ni^{2+} allowing it to bind Ni^{2+} with nanomolar affinity (K_d 0.19 µM). This is the first demonstration of a microplate-based screen for metal-binding activity with SBPs, which is amenable to automation for high-throughput applications.

Keywords

solute binding protein; ABC transporter; metal-binding assay; intrinsic protein fluorescence quenching; tryptophan quenching; ligand titration assay

Short Title

microplate-based screen for metal binding activity

Introduction

Clostridium carboxydivorans P7T is a Gram-positive anaerobic isolate from an agricultural settling lagoon (Stillwater, Oklahoma, USA) and is among a number of clostridium species that scientists and engineers have exploited for solventogenesis and biofuel production.[1–3] Underlying this biotechnology is acetogenesis, an anaerobic process where CO_2 is shuttled into the Wood-Ljungdahl pathway to form acetyl-CoA (Figure 1A).[4] This process is catalyzed by enzymes that have metal co-factor requirements. For example, CO dehydrogenase (CODH) and acetyl-CoA synthase (ACS) possess iron-sulfur clusters that are

bridged to cysteine-coordinated NiFe or NiNi binuclear centres, respectively. In addition, cobalt-bearing vitamin B_{12} is used by the corrinoid iron-sulfer protein (C-FeSP).[4] This implies *C. carboxydivorans* needs a metal acquisition system to capture nickel and cobalt for loading into and activation of these enzymes for acetogenesis to occur. Bacterial metal acquisition systems are well-studied from an animal and human health perspective because pathogen virulence frequently depends on the availability of metals in the host, especially in the gastrointestinal tract.[5] To compete with the host immune system and other members of the gut microbiota that also need these metals to flourish, pathogens use highly specific metal importers known as ATP-binding cassette (ABC) transporters.[6] The canonical ABC transporter has five components: the extracytoplasmic solute binding protein (SBP) that is free floating in the periplasm of Gram-negative bacteria or tethered to the lipid membrane in Gram-positive bacteria, the permease dimer that forms the translocation channel across the lipid membrane, and the cytoplasmic nucleotide-binding domain (NBD) dimer that transforms the chemical energy from ATP hydrolysis into mechanical energy to import metals.[7]

The specificity of metal ABC transporters is derived from the SBP component, which contains the binding site for the target metal ion. NikA from the *Escherichia coli* nickel ABC transporter, NikABCDE, is the best studied nickel-specific SBP (Ni-BP) with extensive biochemical and structural characterization.[8–16] Other Ni-BPs have also been studied because of their implications in health, and include the pathogens *Campylobacter jejuni* (*Cj*NikZ)[17,18], *Brucella suis* (*Bs*NikA)[18,19], *Yersinia pestis* (*Yp*YntA)[18], *Staphylococcus aureus* (*Sa*NikA, *Sa*CntA)[20], *Helicobacter hepaticus* (*Hh*NikA)[21], *Helicobacter pylori* (CeuE)[22], *Vibrio parahaemolyticus* (*Vp*NikA)[23], and *Clostridium difficile* (*Cd*OppA)[24]. In contrast, *C. carboxidivorans* is not known to be pathogenic, but possesses a cluster of coding sequences herein termed the acetogenesis/nickel acquisition (*ana*) operon that encodes for a putative ABC transporter and potential acetogenesis-related enzymes (Figure 1B). The ABC transporter possesses two SBPs, herein termed *Cc*SBPI and *Cc*SBPII, which are both homologous to *Cj*NikZ (41% and 37%, respectively). From this observation, it was hypothesized that the *ana* operon expresses a metal ABC transporter that could import the nickel and cobalt to maturate CODH, ACS, and C-FeSP to their functional forms.

Determining the binding specificity and affinity of SBP components for various ligands can be done *in vitro* using several techniques that have been applied to the aforementioned Ni-BPs: isothermal titration calorimetry (ITC), surface plasma resonance (SPR), and intrinsic protein fluorescence quenching (IPFQ). While ITC and SPR are best used for applications requiring higher accuracy and precision, they are not amenable to screening applications due to their low-throughput nature. IPFQ is more amenable to screening because it relies on changes in the protein's own fluorescence that can be detected in ligand titration assays (LTAs) with a spectrophotometer equipped with fluorescence reading capabilities. For previously studied Ni-BPs, IPFQ has only been used in cuvette format to perform LTAs, which is not amenable to screening applications because the user is limited to a single LTA replicate at a time.

This paper first describes a two-step protein purification workflow to obtain pure *Cc*SBPII with a low metal-protein ratio and free of the 6xHisTag. To study *Cc*SBPII, a multiplex IPFQ-LTA workflow using a 96-well plate was then developed to characterize the binding affinity profile of *Cc*SBPII from the *ana* operon under acidic and alkaline conditions (pH test), a 1000-fold range of NaCl and KCl (salinity test), and with various chelated and non-chelated metal ligands (promiscuity, chelator, and L-histidine tests). Notably, we found that *Cc*SBPII has a micromolar affinity (K_d) for cobalt (Co^{2+}), nickel (Ni^{2+}), and copper (Cu^{2+}), in order of increasing affinity (lower K_d). This suggests that although *Cc*SBPII is similar to *Cj*NikZ (37% ID), which is known to bind Ni^{2+}, *Cc*SBPII exhibits metal promiscuity that may lead to ineffective nickel acquisition *in vivo* by *C. carboxidivorans*. However, in the presence of L-histidine, *Cc*SBPII binds to nickel with low nanomolar affinity, which was 81- and 18-fold stronger than Cu^{2+} in the absence and presence of L-histidine, respectively. Our results demonstrate that *Cc*SBPII has binding activity for several divalent metal ions, but can distinguish between them using L-histidine. This likely allows the *ana* operon's ABC transporter to capture nickel needed to maturate Wood-Lungdahl enzymes for acetogenesis (Figure 1).

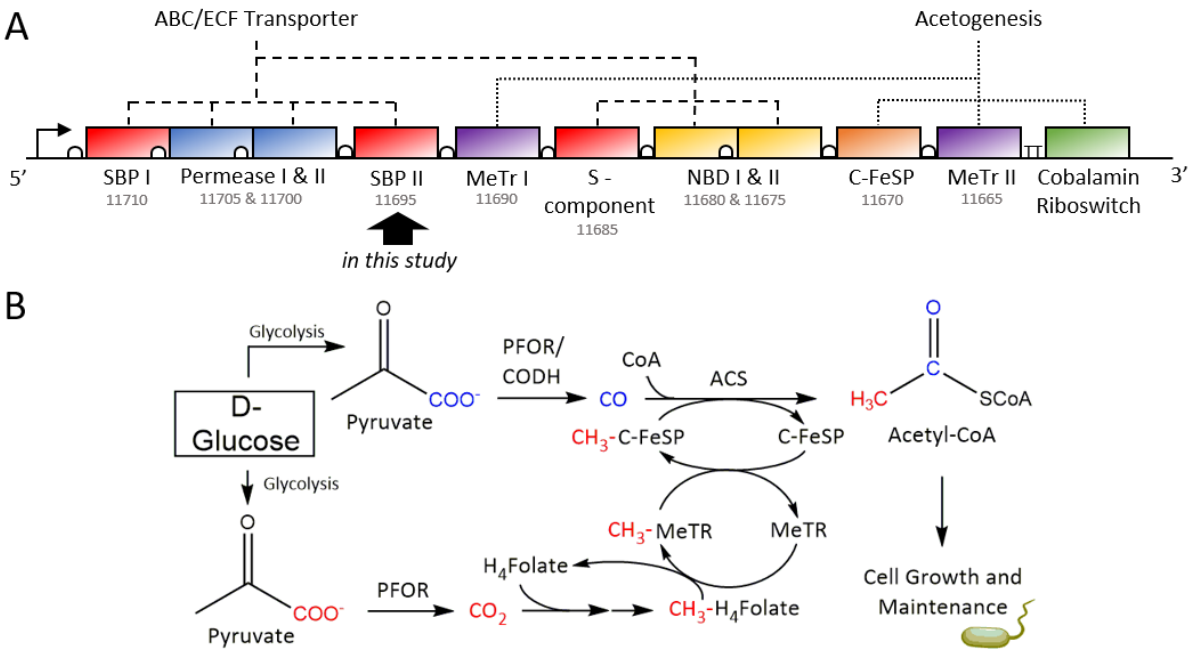

Figure 1. Schematic diagram of the *ana* operon from *Clostridium carboxidivorans* encoding a potential acetogenesis pathway. (A) The *ana* operon is comprised of two sets of coding sequences. The first encodes an ABC transporter, which includes two solute binding proteins (SBP I and SBP II), two permease units (Permease I and Permease II), two nucleotide-binding domains (NBD I and NBD II), and an energy-coupling factor S-component. The second encodes acetogenesis-related enzymes, which includes two methyltransferases (MeTR I and MeTR II), one C-FeSP, and a cobalamin riboswitch after the transcriptional terminator (TT). A promoter (right angle arrow) and ribosome binding sites (white semi-circles) indicate where the operon and coding sequences start, respectively. Numbers below coding sequence names are identifiers that can be prefixed with "Ccar_" to locate them in the *C. carboxidivorans* genome (NZ_CP011803.1). SBP II (*Cc*SBPII) is the protein of interest in this study. (B) Pyruvate is largely derived from glycolysis and possesses a carboxylate group (COO^-) noted in blue and red, representing the Western and Eastern branches of the Wood-Ljungdahl pathway, respectively. Numerous enzymes require metal co-factors. PFOR requires a [4Fe-4S] cluster. CODH requires a [3Fe-4S] cluster bridged to a binuclear NiFe cluster. ACS requires a [4Fe-4S] cluster bridged to a binuclear NiNi cluster. C-FeSP requires cobalamin.

Materials and methods

Bioinformatics of the ana operon and CcSBPII

The *ana* operon of *C. carboxidivorans* was discovered through a blastp search using the *Cj*NikZ open-reading frame (UniProt ID: A0A0M4UJ91), and can be found here: tiny.cc/ccanaoperon. The locations of the promoter, ribosome binding sites, and transcriptional terminator were predicted using BPROM[25], RBS Calculator[26], and FindTerm[25], respectively. The cobalamin riboswitch was predicted using Riboswitch Scanner.[27] Multiple sequence alignments were made and visualized on JalView using the MUSCLE algorithm with default settings.[28] The 3D structure of *Cc*SBPII was made using SWISS-MODEL with unliganded *Cj*NikZ as the template (PDB ID: 4OET), and visualized on PyMOL.[18,29]

DNA synthesis, cloning, and strains

The open-reading frame encoding *Cc*SBPII from *Clostridium carboxidivorans* P7T (Ccar_RS11695, NCBI ID: NZ_CP011803.1) was synthesized (Twist Bioscience, San Francisco, USA) without the start codon and without its native signal peptide (5'-MNKKKITSIVLSCMLVVSVVFT-3'), which was identified using SignalP 5.0 with the Gram-positive setting.[30] The open-reading frame of *Cc*SBPII was cloned into the

expression vector p15TV-L (AddGene ID: 26093) under the T7 promoter and in-frame with the N-terminal 6xHisTag (Twist Bioscience). This construct, found here: tiny.cc/SBPII_anaoperon, was transformed into the *E. coli* expression strain LOBSTR (Kerafast, #EC1001) and plated onto LB-Agar (carbenicillin, 100 µg/mL). The plasmid was miniprepped (GeneAid, #PD300) into MilliQ water and sequence verified at the ACGT Sequencing Facility (Toronto, Canada). Glycerol stocks were prepared for storage at -80 °C.

Large scale protein expression and two-step protein purification and TEV cleavage

Starter cultures were grown from glycerol stock in LB with carbenicillin (100 µg/mL) for 16 hrs overnight at 37 °C with shaking. Expression cultures were started by pre-warming TB media with 5% glycerol and carbenicillin (100 µg/mL) to 37 °C before 1% v/v inoculation with the starter culture, then grown for 3 hrs at 37 °C until addition of IPTG (BioShop, #IPT002) to 0.4 mM for induction. The expression cultures were then transferred to 16 °C and grown for 16 hrs overnight with shaking, then pelleted with centrifugation and transferred to conical vials for one freeze-thaw cycle at -20 °C.

Frozen cell pellets were thawed and resuspended in binding buffer (10 mM HEPES, 500 mM NaCl, 5 mM imidazole, pH 7.2) to a final volume of 100 mL, followed by addition of 0.25 g lysozyme (BioShop, #LYS702). Cell pellet mixtures were sonicated for 25 min (Q700 Sonicator, Qsonica) and clarified by centrifugation. The soluble layer (supernatant) was applied to a cobalt-charged (Co-)NTA resin (ThermoFisher, #88221) pre-equilibrated with binding buffer in a gravity-column set-up. Bound proteins were cleansed with 100 mL of wash buffer (10 mM HEPES, 500 mM NaCl, 25 mM imidazole, pH 7.2) and the bound protein was collected using 10 mL of elution buffer (10 mM HEPES, 500 mM NaCl, 250 mM imidazole, pH 7.2). Protein concentrations were determined by Bradford assay and protein purity was determined by SDS-PAGE analysis and densitometry on Image Lab (Bio-Rad).

Eluted protein was combined with 0.4 mg of in-house purified TEV protease and TCEP to 1 mM (BioShop, #TCE101), then transferred to a 10 kDa MWCO dialysis bag (ThermoFisher, #68100) for dialysis in 4 L dialysis buffer (10 mM HEPES, 1 mM TCEP, 1g/L Chelex 100, pH 7.2) at 4 °C with gentle stirring for 72 hrs. Dialyzed samples were then applied to a cobalt-charged NTA resin twice and concentrated to 2 mL by centrifugation using 30 kDa MWCO concentrators (Millipore Sigma, #GE28-9323-61). This concentrate was applied to a MonoQ 5/50 anion exchange resin (GE Healthcare, #17516601) using 10 mM HEPES, pH7.2 for the mobile phase, and 10 mM HEPES, 1M NaCl, pH 7.2 for elution. Eluted proteins were collected in 96 deep-well blocks and stored at 4 °C during SDS-PAGE analysis. Selected fractions with sufficient purity were transferred to a 10 kDa MWCO dialysis bag for dialysis in dialysis buffer (10 mM HEPES, pH 7.2) at 4 °C with gentle stirring for 24 hrs. They were then diluted to 1 mg/mL with 10 mM HEPES, pH 7.2 and flash-frozen drop-wise with liquid nitrogen before storage at -80 °C.

Matrix-assisted laser desorption/ionization time-of-flight (MALDI-ToF)

Matrix solution (30% v/v ACN, 0.05% v/v TFA , sinapinic acid to saturation) was briefly centrifuged to remove undissolved sinapanic acid, then combined with 1 µL of 1 mg/mL *Cc*SBPII in a 1:1 ratio and applied to a polished steel target plate (Bruker, Part No. 8281817) to dry at room temperature. The Bruker Microflex LT MALDI-ToF was used in the 20 – 100 kDa range to analyze the ACN:TFA-*Cc*SBPII precipitate by collecting 200 shots with the laser at 85% power and 60 Hz. Data was analyzed on flexAnalysis v3.4.

Inductively-coiled plasma mass spectrometry (ICP-MS)

A multi-element standard curve (Millipore Sigma, #1094800100) was prepared (0, 0.01, 0.1, 0.5, 1, 5, 10, 15, and 20 ppb) volumetrically in MilliQ water, each containing a final concentration of 2% TraceMetal™ Grade HNO_3 (ThermoFisher, #A509P500) and 8 ppb TraceCERT® germanium (Millipore

Sigma, #05419) for the internal standard. *Cc*SBPII samples for metal analysis were prepared in the same manner with a final *Cc*SBPII concentration of 0.67 µM (total volume = 3 mL per *Cc*SBPII sample). For metal analysis, the ICP-MS (Thermo-Fisher X-Series 2) was equilibrated at 20 °C for 30 min. The system was then flushed with 2% TraceMetal™ Grade HNO_3 for 30 min and tuned using the tune A solution (Fisher Scientific, #NC9063415). Triplicates were acquired and processed automatically by PlasmaLab, then visualized using GraphPad Prism 5.0.

Circular dichroism (CD)

The JASCO-800 spectropolarimeter was flushed with nitrogen gas (20 L/min) for 15 min and allowed to equilibrate at 25 °C with running distilled water before turning the lamp on. A 1-mm quartz cuvette (Millipore Sigma, #Z800015) was washed with MilliQ water, 70% EtOH, 70% HNO_3, and a final wash with MilliQ water. 1 µM of purified *Cc*SBPII in MilliQ water was added to the cuvette and analyzed in triplicate using the Measurement Mode between 180 – 260 nm at a 1 nm interval. The curve was then smoothed using a Savitzky-Golay filter on CAPITO[31], then visualized using GraphPad Prism 5.0.

Intrinsic protein fluorescence quenching – ligand titration assay (IPFQ-LTA)

IPFQ experiments for excitation and emission spectra of 0.25 µM bovine serum albumin (Millipore Sigma, #P0834) and 0.25 µM *Cc*SPII were performed in a 10-mm quartz cuvette (Hellma, #104-10-40) on the SpectraMax M2 spectrophotometer (Molecular Devices). IPFQ-LTAs were performed in black, opaque 96-well microplates (Greiner Bio-One, #655076) using the same spectrophotometer with the following settings: top-read, 25 °C, λ_{ex} 280 nm, λ_{em} 380 nm, PMT high, sensitivity 30, carriage speed high, 5 s shaking before endpoint reads, and shaking in between reads during kinetic reads. For all IPFQ-LTA tests, *Cc*SBPII was combined with activity buffer (10 mM HEPES, pH 7.2) to 0.25 µM *Cc*SBPII (200 µL total in a well) and allowed to equilibrate in the spectrophotometer for 20 min with shaking. Unless otherwise specified, ligands were prepared to 1 mM in activity buffer. After equilibration, aliquots of the ligands are added in stepwise fashion using a multichannel pipette up to a maximum of 100-120 µL. Each aliquot addition was followed by a 3 min equilibration with shaking before endpoint reads were made. IPFQ-LTAs were done in triplicate in addition to a negative control triplicate where *Cc*SBPII was titrated with only activity buffer (no ligand).

In the IPFQ-LTA for non-specific binding of Ni^{2+} to protein surfaces, 0.25 µM of *Cc*SBPII, bovine serum albumin (Millipore Sigma, # A9418) and lysozyme (BioShop, #LYS702) were titrated with 1 mM $NiSO_4$. In the promiscuity test, reagents of at least 97% purity were used to make ligand solutions for $NiSO_4$, $CoCl_2$, $CuCl_2$, $ZnCl_2$, $MnCl_2$, and $CdCl_2$. In the chelator and L-histidine test, complexes were made according to their stoichiometry. For example, Ni-$(His)_2$ would require a 1:2 stoichiometric ratio between Ni^{2+} and histidine (*i.e.* 1 mM Ni^{2+} and 2 mM histidine to make 1 mM Ni-$(His)_2$. In this fashion, 1 µM solutions were made for L-histidine (herein termed His), Ni-$(His)_2$, Co-$(His)_2$, Cu-$(His)_2$; 20 µM solutions for His, Co-$(His)_2$ and Cu-$(His)_2$; and 1 mM solutions for Ni_2-$(Citrate)_2$, Ni-EDTA, Ni-DETA, citrate (2 mM), EDTA, and DETA (Millipore Sigma, # D93856).

In the pH and salinity test, the activity buffer was modified to have pH values of 2.5, 6.8, 7.2, 8.5 (adjusted with HCl and NaOH); and 0.01 M, 0.1 M, 1M NaCl or KCl. The buffer for the ligand, $NiSO_4$ in these cases, remained at 10 mM HEPES, but the pH or salt concentrations were modified to match the cognate activity buffer (*e.g.* 10 mM HEPES, 0.1 M KCl, pH 7.2 activity buffer is titrated with 1 mM $NiSO_4$, 10 mM HEPES, 0.1 M KCl, pH 7.2). Raw data was processed by first averaging the relative fluorescence units (RFU, arbitrary units, a.u.) for a set of IPQF-LTA replicates (either ligand test or negative control) at each titration step (stage 1). The averaged negative control data was then subtracted from the averaged ligand test data at each titration step to normalize the data (stage 2). Finally, the data was blanked by subtracting the RFU

value just before the first titration step from the RFU values of the subsequent titration steps (stage 3). Standard deviation is calculated for stage 1 data, and error propagation is applied to stage 2 data to account for the subtraction of two means. The data was then fitted using a 1:1 binding model (Equation 1,2) in a non-linear regression solver (Excel) and visualized using GraphPad Prism 5.0.

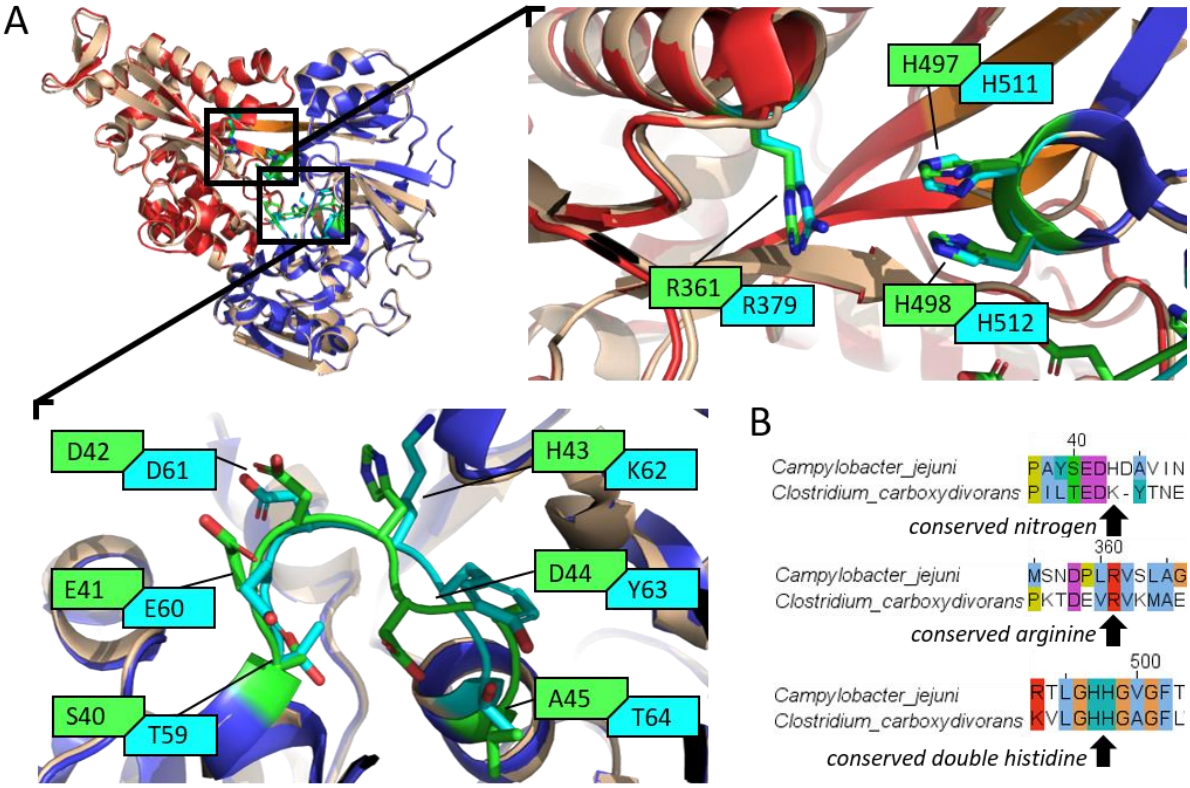

Figure 2. Similarities between *Cj*NikZ and *Cc*SBPII revealed by structural and sequence analysis. (A) A superimposition was made on PyMOL using the unliganded *Cj*NikZ structure (tan, PDB ID: 4OET) and the predicted *Cc*SBPII structure (red - Western lobe, blue - Eastern lobe, orange - hinge region) from SWISS-MODEL with 4OET as the template. The top-right panel (RHH cavity) and bottom-left panel (variable loop) are zoom-ins of the superimposition and highlight residue similarities and differences between *Cj*NikZ (green residues) and *Cc*SBPII (cyan residues). (B) A multiple sequence alignment reveals *Cc*SBPII uses K62 instead of H43 from *Cj*NikZ, but has conserved binding residues otherwise (black arrows).

Results & Discussion

CcSBPII expression, purification, and validation

*Cc*SBPI and *Cc*SBPII were discovered while creating a library of *Cj*NikZ homologs through a Blastp search using the *Cj*NikZ open-reading frame as a query. *Cc*SBPII was selected for this study because it was readily solubilized first. *Cc*SBPII was found to share 37% sequence identity to *Cj*NikZ. *Cc*SBPII's function was first investigated with homology modelling to predict its structure on SWISS-MODEL[29] using unliganded *Cj*NikZ (PDB ID: 4OET) as the template (Figure 2A). The modelling result of *Cc*SBPII received a GMQE score[32] of 0.75 and a QMEAN[33] score of -2.75 indicating good reliability in the predicted structure. The crystal structure of liganded *Cj*NikZ (PDB ID: 4OEV) reveals binding residues H43, H497 and H498 directly interacting with Ni^{2+}, and R361 interacting with an oxalate molecule that helps coordinate the remaining octahedral geometry of Ni^{2+} (different numbering due to the removal of the signal peptide in Lebrette *et al.* 2014).[18] *Cc*SBPII possesses the same binding residues with the exception of K62 from the

variable loop replacing the H43 from *Cj*NikZ (Figure 2B). We speculate this substitution (His to Lys) may contribute to differences in the binding affinity profile between *Cc*SBPII and *Cj*NikZ.

We were interested in developing a high-throughput detection method for metal-binding activity, so we wanted to complement this with a scalable recombinant protein purification method. Presently, metal affinity chromatography is the most efficient protocol for recombinant protein purification, which often does not require additional purification steps.[34] In our work, we chose to use an NTA resin workflow for immobilized metal-affinity chromatography, but anticipated contamination by metals and non-target metal-binding proteins due to the nature of this method. Therefore, several precautions were taken during *Cc*SBPII's purification to remove these contaminants. First, *Cc*SBPII was expressed in large scale cultures using the *E. coli* expression strain LOBSTR with genetically modified copies of *arnA* and *slyD* resulting in a higher purity of purified target proteins.[35]

Second, *Cc*SBPII's ability to bind to NTA resins charged with cobalt and copper was tested to determine if using a Ni-NTA resin could be avoided, thus minimizing the introduction of nickel to *Cc*SBPII (Figure 3A). We found that Co-NTA had comparable performance to Ni-NTA based on the size of the bands produced on the SDS-PAGE analysis, so we proceeded to use Co-NTA for all further purifications.

Overall, *Cc*SBPII was purified to approximately 98% purity (Table 1) through a combination of purification techniques (Figure 3B). Following Co-NTA purification, a 72-hr dialysis step was performed where TEV protease was added to cleave the 6xHisTag from *Cc*SBPII, and Chelex 100 was added to the dialysis buffer to remove excess nickel in the solution. MALDI-ToF was used to confirm the completeness of TEV cleavage (Figure 4A). Based on the open-reading frame, *Cc*SBPII is expected to have a molecular weight of 57,269 Da, but 59,694 Da with the inclusion of the 6xHisTag and TEV cleavage site. The observed molecular weights were 55'539 Da and 57'893 Da, respectively, which are approximately 1750 Da lower than the theoretical values. This discrepancy is explained by which part of the peak one decides to use for analysis. One could use the centre of the peaks, which would align better with the theoretical molecular weights in this case. For *Cc*SBPII, the maximum peak of each spectrum was used instead, revealing a difference of 2'354 Da.

Table 1. *Cc*SBPII purification and purity profile

	mg/mL	mg	Purity
Cell Lysate	83.8		23%
Wash-120 mL	0.2		
Elution Fraction 1	1.1		69%
Elution Fraction 5	0.1		
1st Co-NTA Elution Combined	0.5	5	
Post-dialysis + 2nd Co-NTA	0.4		
Pre-aEX concentrate	1.6	3.2	
Elution Fraction D2	0.5		98%
Elution Fraction E3	0.9		99%
Post-IEX Elution Combined	1.0	2.2	>98%

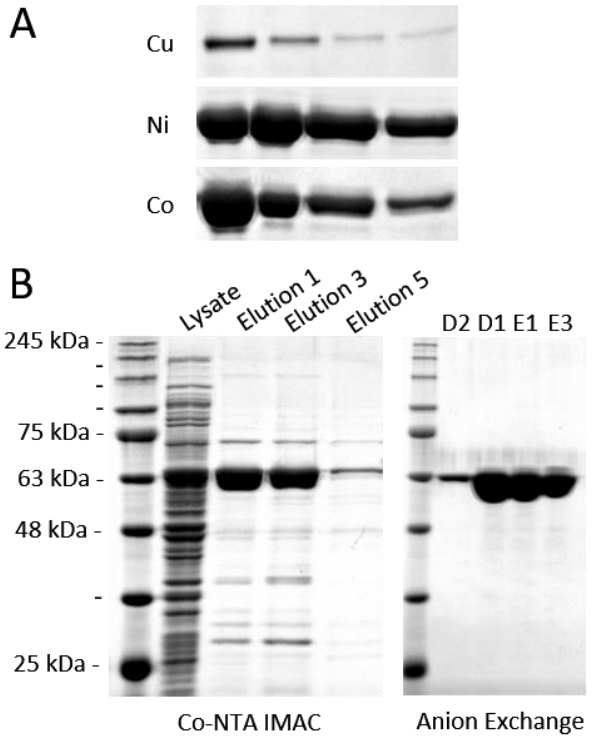

Figure 3. SDS-PAGE analysis of *Cc*SBPII purification. (A) A comparison of *Cc*SBPII purification using NTA resin charged with copper, nickel, and cobalt. (B) Two-step purification of SBPII. Left-panel: 1st step, purification using Co-NTA resin (elution with 250 mM imidazole). Right-panel: 2nd step, purification using anion exchange chromatography on MonoQ to remove remaining impurities.

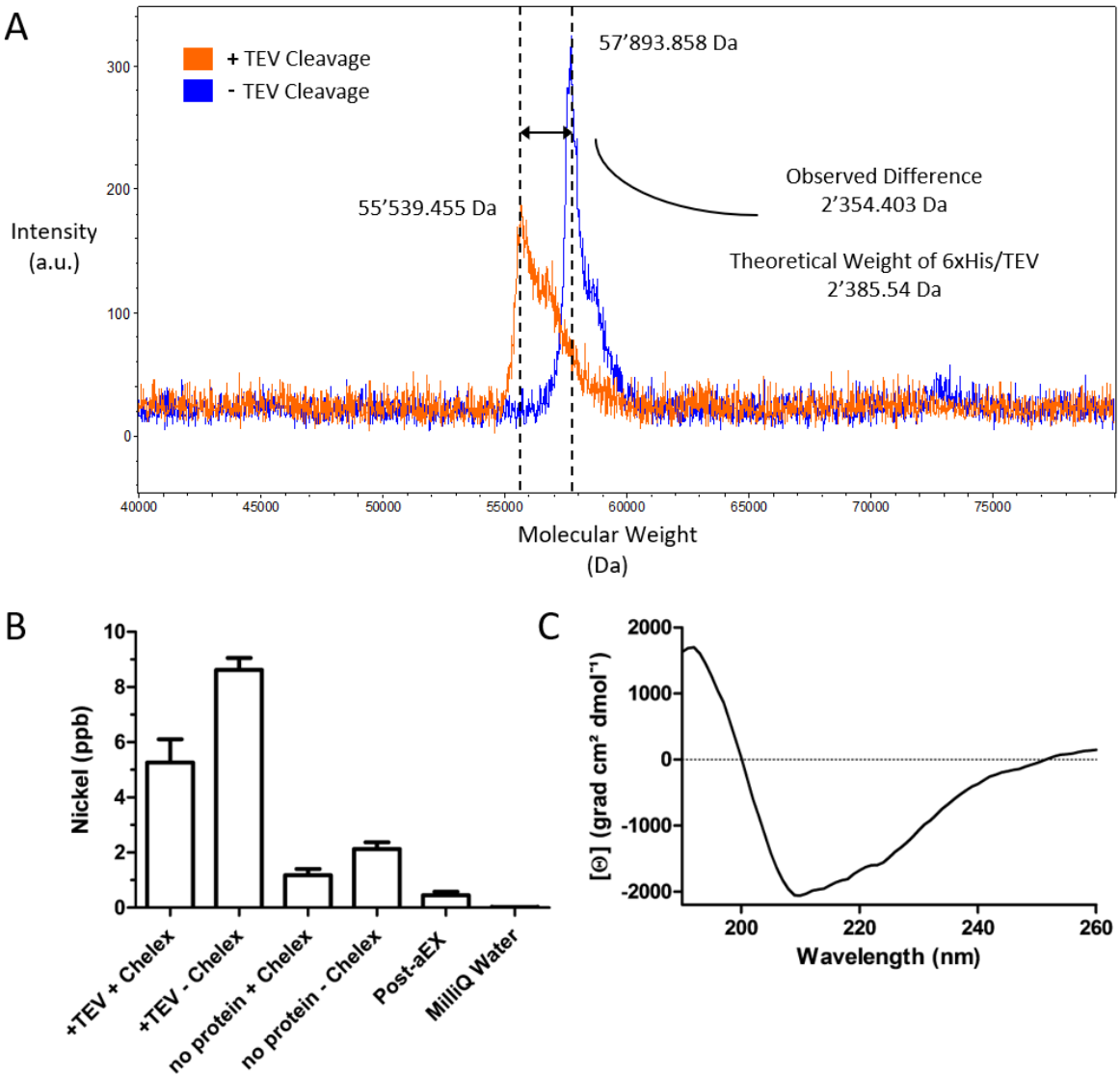

Figure 4. Post-purification validation of tag removal, nickel removal, and proper protein folding of purified *Cc*SBPII. (A) MALDI-ToF analysis of protein molecular weight with two samples (orange – addition of TEV, blue – no addition of TEV). Dashed black lines depict the maximum peaks for each sample. (B) ICP-MS analysis of nickel concentration to evaluate the usage of Chelex 100 to remove heavy metals from the Co-IMAC protein eluent, which is collected after applying the cell lysate to the Co-NTA and washing the resin with washing buffer. This protein eluent is combined with TEV for cleavage and dialyzed for 72 hrs with and without Chelex 100, labelled "+TEV +Chelex" and "+TEV +Chelex", respectively. A negative control is included where the cell lysate volume is replaced with binding buffer to determine the extent of cobalt released from the resin during Co-IMAC without the presence of proteins. No TEV is added to the eluent in this case and is dialyzed in the same fashion, labelled "no protein + Chelex" and "no protein – Chelex". *Cc*SBPII after the final 24 hr dialysis, prior to freezing, was also evaluated by ICP-MS and labelled "Post-aEX". (C) CD spectrum of *Cc*SBPII after being blanked with 10 mM HEPES, pH 7.2.

The theoretical molecular weight of the 6xHisTag and TEV cleavage site is 2'385 Da, indicating successful removal of this affinity tag from *Cc*SBPII.

Previous studies have used EDTA to remove metal contaminants from the target protein samples, but *Ec*NikA and its homologues have been observed to bind to Ni-EDTA, which we wanted to avoid if this is true for *Cc*SBPII.[14,17,18] ICP-MS was used to evaluate the effectiveness of Chelex 100 at removing nickel from the *Cc*SBPII sample inside the dialysis bag (Figure 4B). After the 72-hr dialysis, we found that it provided a 40% reduction in nickel from 8.6 ppb to 5.3 ppb when *Cc*SBPII was present, and a 43% reduction in nickel from 2.1 ppb to 1.2 ppb when *Cc*SBPII was not present. The dialyzed and cleaved *Cc*SBPII sample

was then passed through a Co-NTA resin twice to remove uncut *Cc*SBPII and any remaining contaminant proteins. Finally, the flow-through was applied to an FPLC with an anion exchange resin (MonoQ) to improve the protein purity and dialyzed once more with Chelex 100 for 24 hr to reduce the concentration of NaCl and any remaining metals. This whole procedure yielded *Cc*SBPII at 2.2 mg/L of culture with a final concentration of 1 mg/mL with 0.5 ppb nickel, representing a 0.01 metal-protein ratio that is recommended by Handing *et al.* 2018 and used in a study that measured metal binding affinity by ITC.[18,36]

Prior to using *Cc*SBPII in IPFQ-LTAs after thawing, the integrity of its secondary structures was evaluated using CD (Figure 4C). We found that it maintained a primarily α-helical conformation, but a peak was missing at 220 nm that is typical of α-helical proteins. This is likely explained by *Cc*SBPII's antiparallel β-pleated sheets found in the core of the Western and Eastern lobes, which can produce a different spectrum that could reduce the steepness of the peaks around 220 nm and 200 nm (Figure 2A). Consequently, the observed CD spectrum for *Cc*SBPII is likely a product of both the α-helices and β-pleated sheet spectra, suggesting that its secondary structures are preserved throughout the purification workflow and after thawing. One batch of purified *Cc*SBPII was used for both the development of the IPFQ-LTA, and characterization of its binding affinity profile with the optimized IPFQ-LTA.

Developing the IPFQ-LTA in 96-well microplate format

IPQF-LTAs in microplate format have been performed for inhibition studies with organic molecules[37,38], but to our knowledge it has not been well-described for Ni-BPs. There are two pre-requisites for IPFQ-LTAs to provide accurate information about a protein's binding parameters: 1) the protein should have tryptophan residues, ideally near the binding sites and 2) the ligand to be titrated should have minimal absorption of light at the λ_{ex} and λ_{em} used in fluorescence reads. *Cc*SBPII contains seven tryptophan residues, two of which (W404 & W419) are located adjacent to the binding site and the other five evenly dispersed across the Western and Eastern lobes (Supplementary Figure 1). We first used fluorescence excitation and emission spectra to compare *Cc*SBPII and BSA's behavior in a quartz cuvette format and a 96-well black opaque microplate format chosen to minimize cross-well interference (Figure 5A). *Cc*SBPII and BSA excite most strongly near 280 nm in both formats. *Cc*SBPII and BSA emitted most strongly at 370 nm in cuvette format, but 380 nm in microplate format, so λ_{ex} 280 nm and λ_{em} 380 nm were used in subsequent fluorescence reads. Notably, the cuvette format produced less resolved spectra than the microplate format for both *Cc*SBPII and BSA, which may reflect its susceptibility to noise.

Initial IPFQ-LTA trials in microplate format did not yield binding curves likely due to protein adsorption to the well and therefore poor homogeneity that resulted in large RFU fluctuations during fluorescence reads. To address this, we tested various shaking regimes and equilibration times (data not shown) and found that *Cc*SBPII needed constant shaking for at least 5 min for the signal to stabilize before an IPFQ-LTA. Overall, the best regime was a 15-20 min "pre-equilibration" period before an IPFQ-LTA, and 3 min equilibration period during an IPFQ-LTA, between each titration step (Figure 5B).

We also found that the initial signal to noise ratio was high, possibly due to minor differences in pipetting between replicates and intrinsic variability with the spectrophotometer, which caused standard deviations to be up to 50% of the signal (data not shown). We addressed this by testing different concentrations of *Cc*SBPII in IPFQ-LTAs with Ni^{2+} and found that 0.025 mg/mL (0.2 µM) of *Cc*SBPII was enough to yield standard deviations that were approximately 10% of the signal (Figure 5C). The magnitude of the standard deviations did not change upon increasing the concentration of *Cc*SBPII, suggesting that the variability does not arise from *Cc*SBPII. To verify that changes in fluorescence throughout the IPFQ-LTAs arose from binding activity and not non-specific adsorption interactions between Ni^{2+} and the outer surface of *Cc*SBPII, 0.25 µM BSA and 0.25 µM lysozyme were also titrated with Ni^{2+} (Figure 5D). We found that neither yielded notable changes in fluorescence in the concentration range tested compared to *Cc*SBPII, which clearly shows quenching of the fluorescence with increasing exposure to Ni^{2+}.

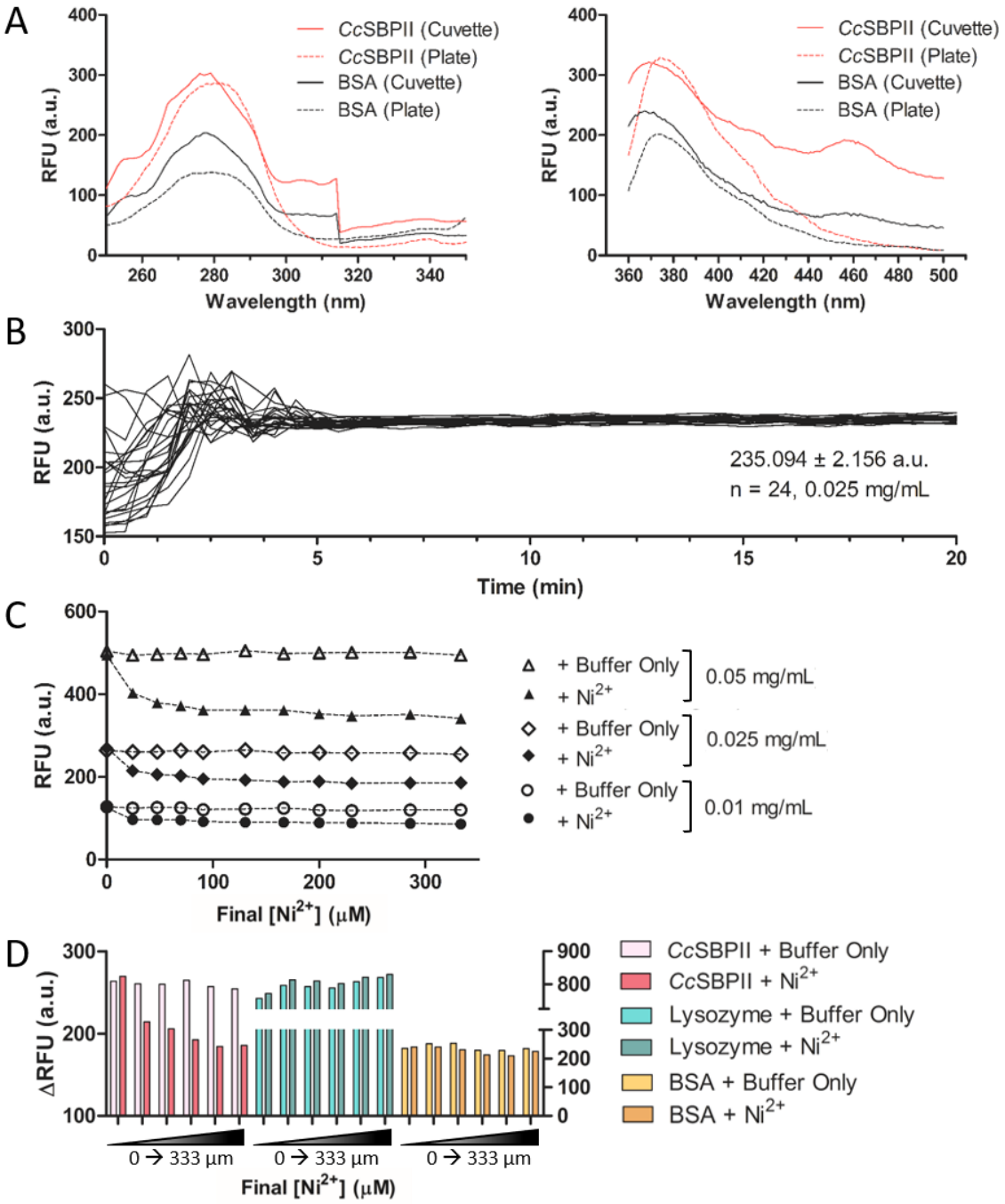

Figure 5. Optimization of IPFQ-LTAs in 96-well microplate format. (A) Comparison of *Cc*SBPII and BSA fluorescence excitation and emission spectrum in cuvette and microplate format. Left-panel: excitation spectrum with λ_{em} set to 380 nm. Right-panel: emission spectrum with λ_{ex} set to 280 nm. (B) Pre-equilibration period of 0.025 mg/mL *Cc*SBPII samples monitored by a kinetic fluorescence read with λ_{ex} 280 nm and λ_{em} 380 nm. (C) Titration of Ni^{2+} and activity buffer (negative control) into 0.05 mg/mL, 0.025 mg/mL, and 0.01 mg/mL *Cc*SBPII. (D) Titration of Ni^{2+} and activity buffer (negative control) into 0.25 μM *Cc*SBPII, BSA, and lysozyme to evaluate non-specific interactions between Ni^{2+} and protein surfaces. Only lysozyme is plotted on the right y-axis.

Inner-filter effect and binding model selection

Precautions were taken in this study to address some common pitfalls in IPFQ experiments, as discussed previously by others.[39,40] Changes in protein fluorescence upon titration of a ligand can be a result of the inner filter effect (IFE) where the ligand absorbs light at the λ_{ex} and λ_{em} used in the

fluorescence reads. We analyzed the UV-Vis absorption spectra for the divalent metals and chelators used in this study, at the maximum concentrations used in the IPFQ-LTAs, by comparing theirs to the activity buffer's (10 mM HEPES, pH 7.2) UV-Vis spectrum. We found that none of the metals or chelators differed from the activity buffer (data not shown). We note that ferrous (Fe^{2+}) and ferric iron (Fe^{3+}) were also tested and showed very strong absorbance compared to the activity buffer, hence why they are not included in this study. Since we used ligand and ligand-chelator concentrations that were at least ten-fold higher than the protein concentration, we assumed the final concentration of the ligand (L_a) in the wells to be equal to the concentration of the ligand available (L_{free}) for binding. From this, we used a 1:1 binding model (Equation 1) in a non-linear regression to determine F_{max} and K_d values.[39,40] For the L-histidine chelator test where the chelator and ligand-chelator concentrations were at points smaller than the *Cc*SBPII concentration in the well, we modified the 1:1 binding model to included the Hill coefficient (Equation 2). F_p is the processed fluorescent reading (stage 3) that was observed. F_{max} is the theoretical maximum change in fluorescence during ligand saturation, which describes the degree of quenching caused by the ligand binding to the protein. K_d is the dissociation constant, which describes the protein's affinity for a ligand. These parameters are summarized in Table 2.

$$(1)\ F_p = \frac{F_{max}\, L_a}{L_a + K_d} \qquad (2)\ F_p = \frac{F_{max}\, L_a^n}{L_a^n + K_d^n}$$

Table 3. Dissociation constants (k_d), F_{max}, and Hill Coefficients from IPFQ-LTA of *Cc*SBP II

		k_d (µM)	F_{max}	Hill Coefficient
Promiscuity Test	Ni^{2+}	32.6	56.9	
	Co^{2+}	142.6	48.9	
	Cu^{2+}	12.2	218.7	
	Zn^{2+}	n/a	n/a	
	Mn^{2+}	n/a	n/a	
	Cd^{2+}	n/a	n/a	
	Fe^{2+}	n/a	n/a	
pH Test	2.5	217.1	32.1	
	6.8	68.9	45.5	
	7.2	28.1	66.6	
	8.2	22.1	76.8	
NaCl Test	0.01 M	64.5	82.9	
	0.1 M	103.0	57.1	
	1 M	151.1	38.9	
KCl Test	0.01 M	44.2	57.3	
	0.1 M	102.9	38.9	
	1 M	424.7	69.4	
Chelator and L-histidine test	Ni_2-$(Citrate)_2$	28.0	60.9	
	Ni-EDTA	218.7	129.0	
	Ni-DETA	121.8	72.5	
	Citrate	n/a	n/a	
	EDTA	n/a	n/a	
	DETA	n/a	n/a	
	Ni-$(His)_2$	0.19	203.4	1.4
	Cu-$(His)_2$	2.7	90.6	2.3
	Co-$(His)_2$	1.7	162.0	1.3

n/a - indicates where the non-linear regression could not obtain values due to a poor fit between the observed values and the Michaelis-Menten-like equation. Values in blue font are to be interpreted with caution.
* metals that were titrated were at 1 mM, ** His-chelated metals were titrated at 20 µM

Analysis of metal promiscuity

The promiscuity test (Figure 6A,B) explored *Cc*SBPII's ability to bind to divalent metal ions known to form complexes with proteins[41,42]: Ni^{2+}, Co^{2+}, Cu^{2+}, Zn^{2+}, Cd^{2+}, and Mn^{2+}. We observed binding to Ni^{2+} (K_d 32.6 µM), which is less than the reported value for *Cj*NikZ with Ni^{2+} (K_d 1.6 ± 0.2 µM). This difference may arise from the presence of lysine (K62) in the variable loop instead of the histidine that is in *Cj*NikZ (Figure 2). At pH 7.2, which was used in this test, lysine is protonated (pK_a 10.79) so it does not participate in metal-binding. Rather, it destabilizes the protein-metal interaction through charge-charge forces.[43] We also found that *Cc*SBPII binds to Co^{2+} and Cu^{2+} (K_d 142.6 µM and 12.2 µM, respectively), where Cu^{2+} has an F_{max} that is approximately four-fold larger than Ni^{2+}. In the presence of Cu^{2+}, the binding of *Cc*SBPII to Ni^{2+} is inhibited, showing evidence for competition between these two metals (Supplementary Figure 2). The other three metals tested did not yield interpretable binding curves. Cd^{2+} is a much bulkier ion than the other first row transition metals and has a preference for sulfur donor groups and a tetrahedral geometry which *Cc*SBPII does not provide.[42,44] Zn^{2+} and Mn^{2+} could not saturate *Cc*SBPII in the concentration range that was tested, suggesting they are not targets for the cognate ABC transporter. While Zn^{2+} and Mn^{2+} have similar radii to the other first row transition metals, Zn^{2+} has a preference for a tetrahedral coordination geometry and Mn^{2+} generally has weak affinity for proteins.[45,46] Put together, *Cc*SBPII's metal promiscuity reflects the Irving-William series that recapitulates determinants for protein-metal-binding affinity into the series $Mn^{2+} < Cd^{2+} < Co^{2+} < Ni^{2+} < Cu^{2+} > Zn^{2+}$.[46,47] This promiscuity test reveals *Cc*SBPII is selective for Co^{2+}, Ni^{2+}, and Cu^{2+} in order of increasing affinity, which suggests the cognate ABC transporter is a copper-specific importer. However, our chelator tests suggest otherwise.

Analysis of chelator utilization

The chelator test (Figure 6C) explored *Cc*SBPII's ability to bind to complexes of Ni^{2+} with two organic chelators previously studied in Ni-BP binding assays: citrate and EDTA. Additionally, DETA is a flotation reagent used in hydrometallurgical processes and was also tested to gauge *Cc*SBPII's ability to bind to environmental contaminants. We found that *Cc*SBPII binds to all three complexes (K_d 28.0 µM, 218.7 µM, and 121 µM, respectively), whereas the control with titration of the chelator without the Ni^{2+} produced no hyperbolic curves. Of note, *Cc*SBPII's ability to bind to Ni^{2+} chelated by EDTA and DETA raises questions about whether these chelators are also translocated through the permease dimer of the cognate ABC transporter and into the cytoplasm where they could be metabolized. L-histidine was also tested in the same concentration range used for these chelators, but saturation occurred almost immediately in the second titration step (data not shown), which lead us to probe whether *Cc*SBPII was able to use this chelator to specifically bind to Ni^{2+}, rather than Co^{2+} and Cu^{2+}, at a sub-micromolar range.

The L-histidine test (Figure 6D,E) explored *Cc*SBPII's ability to bind to complexes of Ni^{2+}, Co^{2+}, and Cu^{2+} with L-histidine molecules (generally termed M-(His) where "M" is for the divalent metal ion). The M-(His) solutions are prepared before IPFQ-LTAs such that the molar stoichiometry is 1:2 between the metals and L-histidine, therefore making M-$(His)_2$ complexes. This was to ensure all three metals could form their preferred octahedral coordination geometries. We first tested binding in the low nanomolar range and found *Cc*SBPII was able to bind to Ni-$(His)_2$ (K_d 0.19 µM) and not the other complexes or L-histidine alone. We then tested binding in the very low micromolar range and found *Cc*SBPII was able to bind to Co-$(His)_2$ and Cu-$(His)_2$ (K_d 1.7 µM and 2.7 µM, respectively). The presence of L-histidine enhances *Cc*SBPII's ability to bind to Ni^{2+}, Co^{2+}, and Cu^{2+} by a factor of 171, 80, and 4, respectively. Moreover, *Cc*SBPII binds to Ni-$(His)_2$ and Co-$(His)_2$ stronger than Cu-$(His)_2$ by a factor of 14 and 1.6, respectively. This represents a reversal of the binding preference shown for bare Ni^{2+}, Co^{2+}, and Cu^{2+} without chelators, which suggests *Cc*SBPII overcomes Cu^{2+} competition by using L-histidine in a similar fashion to intestinal pathogens that use siderophores and siderophore-like molecules to out-compete host defense systems.[48,49] We postulate

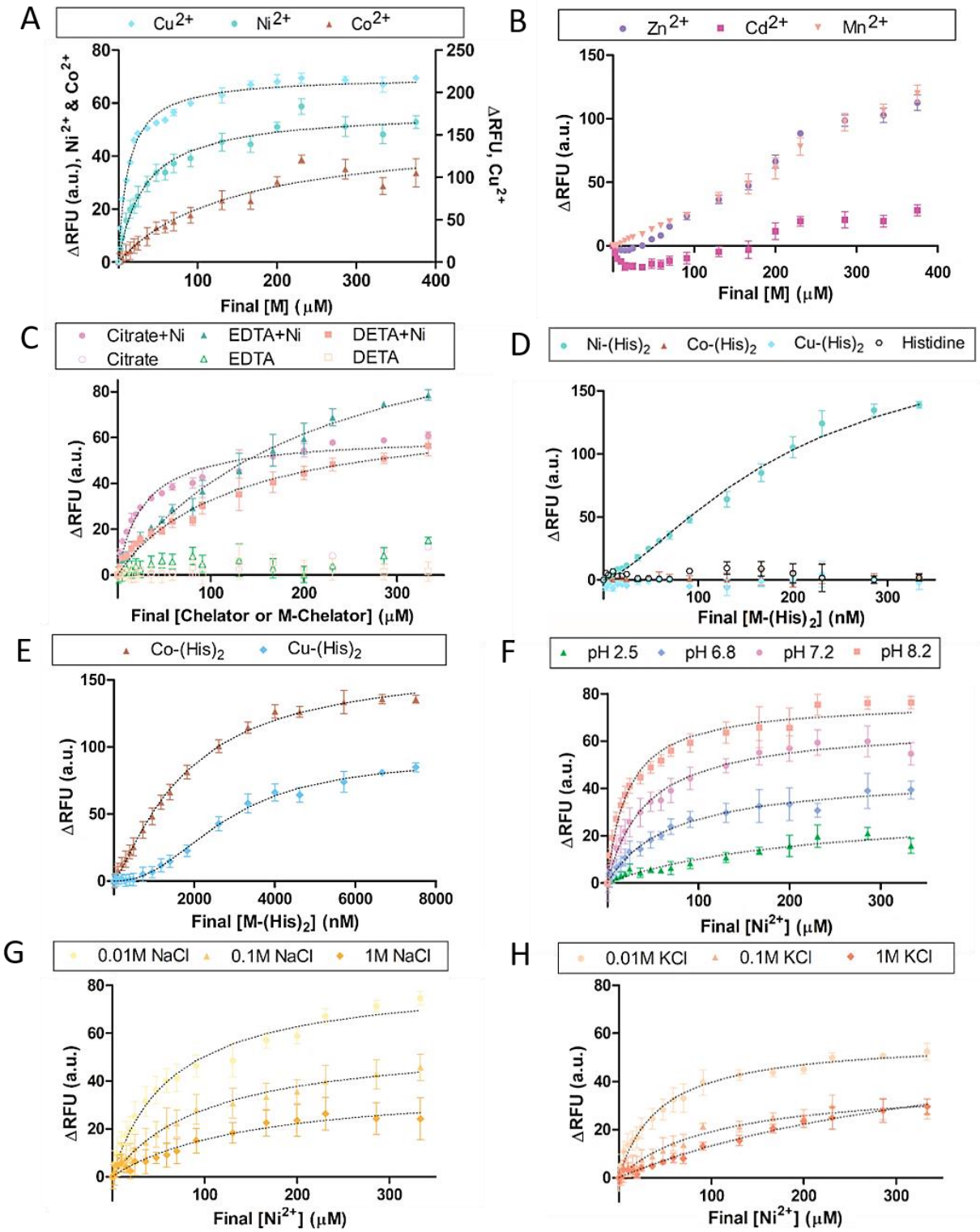

Figure 6. IPFQ-LTA of *Cc*SBPII with various chelated and non-chelated divalent metals. CcSBPII binds to Ni^{2+} under various conditions and exhibits promiscuous binding activity. All data were collected in at least triplicates. "M" refers to divalent metal ions. "Chelator" refers to citrate, EDTA, and DETA. Dotted lines are non-linear regressions fitted to Equation 1, except for (D-E) which were fitted to Equation 2. (A) & (B) Promiscuity test. (C) Chelator test. (D) L-histidine test, nanomolar range. (E) L-histidine test, low micromolar range. (F) pH test. (G) & (H) Salinity test.

*Cc*SBPII possesses a second coordination sphere that may be enhancing its ability to bind to Ni^{2+} and Co^{2+} by orienting its metal-binding residues to accommodate chelators like L-histidine.

A limitation of the IPFQ-LTA is its ability to precisely elucidate the mechanism of binding between the ligand and the protein. While *Cc*SBPII exhibits a large change in fluorescence with nanomolar concentrations of Ni-$(His)_2$, it is an assumption that it binds to Ni^{2+} in complex with two molecules of L-histidine. The structure of *Cj*NikZ binding a single Ni^{2+} and a single L-histidine molecule (PDB ID: 4OEU) contrasts with other structures like *Ec*NikA (PDB ID: 4I8C) and *Yp*YntA (PDB ID: 4OFL) that bind to a single Ni^{2+} complexed with two L-histidine molecules. From just the L-histidine chelator test, it is unclear what exact complex *Cc*SBPII is binding to. However, *Cc*SBPII exhibited slightly sigmoidal binding curves for Ni-$(His)_2$ and Co-$(His)_2$ with Hill coefficients of 1.6 and 1.4, respectively and a relatively large Hill coefficient of 2.3 for Cu-$(His)_2$. Analytical size exclusion chromatography with *Cc*SBPII revealed these Hill coefficients do not arise from oligomerization of the protein (data not shown), likely indicating that there may be multiple binding events present when the concentration of the ligand and chelators are at least an order of magnitude less than the concentration of *Cc*SBPII. These deviations from hyperbolic behavior may provide insight into the mechanism of binding. For example, it may be the case that *Cc*SBPII can only bind to M-(His) or M-$(His)_2$ complexes. It is known that Cu^{2+} is in equilibrium with multiple complexes of L-histidine other than Cu-(His) and Cu-$(His)_2$, which decreases the availability of preferred complexes in solution that *Cc*SBPII can readily bind.[50] This would be an issue at very low nanomolar concentrations of Ni^{2+} and L-histidine where the concentration of *Cc*SBPII is approximately two orders of magnitude larger. Overall, the chelator test reveals *Cc*SBPII's promiscuity is not limited to bare divalent metal ions, but also chelators, which appears to be an advantage that allows it to use L-histidine to very specifically bind to Ni^{2+}. In addition to what *Cc*SBPII binds to, IPFQ-LTAs can reveal its optimum operational window.

Analysis of pH and salinity effects

The pH test (Figure 6F) explored *Cc*SBPII's ability to bind to Ni^{2+} at an acidic pH of 2.5 and circumneutral pH of 6.8, 7.2, and 8.2, chosen intentionally to avoid the isoelectric point of *Cc*SBPII (pH 5.8) and the precipitation of nickel-hydroxides beginning at pH 8.5. We found that increasing alkalinity of the activity buffer decreased the K_d and increased the F_{max}, meaning that stronger binding occurred with more alkaline conditions. This may be attributed to two phenomena. First *Cc*SBPII's histidine residues (pK_a 6.04) that participate in metal-binding are more likely to be deprotonated with increasing concentrations of hydroxides, leading to more charge transfer between the imidazole nitrogen to Ni^{2+}. Additionally, the lysine residue (K62) of the variable loop can be deprotonated by approximately an order of magnitude, which may allow it to begin participating in metal-binding, though this may only be a small contribution. Second, *Cc*SBPII likely requires hydroxides to complete the octahedral coordination geometry that Ni^{2+} prefers, so the increased presence of hydroxides in more alkaline conditions could help.

The salinity test (Figure 6G,H) explored *Cc*SBPII's ability to bind to Ni^{2+} in the presence of NaCl and KCl. We found that increasing the concentration of both salts decreased K_d and F_{max}, meaning that weaker binding occurred at molar level salt concentrations. However, *Cc*SBPII binding to Ni^{2+} in the presence of 0.01 M NaCl had a higher $_{Fmax}$ than the case without any salt present. We speculate a low concentration of NaCl allowed the surface of the *Cc*SBPII protein to be stabilized by Na^+. This would allow *Cc*SBPII to adopt a more compact structure where tryptophan quenching by Ni^{2+} was more effective, leading to greater changes in fluorescence as Ni^{2+} was titrated. However, the general decrease in *Cc*SBPII's ability to bind to Ni^{2+} with increasing salinity is likely a consequence of an increase in ionic strength that causes the activity coefficients for Ni^{2+} and *Cc*SBPII to deviate from 1 (non-ideal conditions). This raises questions about how the activity buffer for IPFQ-LTAs and other techniques should be designed to characterize a protein's binding affinity profile: conditions that better match physiological conditions, or conditions that are as close to pure water as possible to capture a signal derived from only the protein of interest.

Conclusions

The work presented here demonstrates that *Cc*SBPII from *C. carboxidivorans* is indeed a Ni-BP with additional interactions for Co^{2+} and Cu^{2+}, suggesting that the cognate ABC transporter is involved with nickel acquisition with some selectivity for Co^{2+} and Cu^{2+}. A method for purifying SBPs using Co-NTA IMAC and aEX, with minimal nickel contamination and 6x HisTag removal, was validated using ICP-MS, MALDI-ToF, and CD. Furthermore, a microplate format IPFQ-LTA was optimized for detecting metal-binding activity with consideration for the IFE. The optimized IPFQ-LTA was then used to determine *Cc*SBPII's binding affinity profile under a variety of pH and salinity conditions, and with chelated and non-chelated divalent metals. Specifically, we found that *Cc*SBPII was able to bind to a DETA-Ni complex, which raises questions about whether Ni-BPs could play a role in capturing metals chelated by flotation reagents from hydrometallurgical processes that can be difficult to remove with traditional methods like chemical precipitation. We also found there exists Cu^{2+} competition with Ni^{2+} for binding to *Cc*SBPII, but the presence of L-histidine reverses this competition such that a nickel-histidine complex can bind more tightly. It is unclear whether it is M-$(His)_2$ (full complex) that is bound to *Cc*SBPII or M-His (partial complex), therefore requiring characterization using ITC and crystallography. Further work is planned to automate the IPFQ-LTA in microplate format for high-throughput screening of putative Ni-BPs.

We envisage the microplate format IPFQ-LTA as a screening method representing a first-approach strategy for characterizing putative metal-binding proteins with different ligands and under varying conditions. From these results, SPR or ITC should then be conducted to obtain more accurate and precise determinations of K_d and binding stoichiometry. Nevertheless, the IPFQ-LTAs performed in this study reveals a possible role for the ABC transporter of the *ana* operon. *Cc*SBPI possesses the same metal-binding residues as *Cj*NikZ (41% sequence identity) and is likely to function similarly to *Cc*SBPII. In addition, the presence of an S-component in the *ana* operon, which is typically found with energy-coupling factor transporters, suggests that the permease unit of the ABC transporter is versatile in its binding partners. Further studies should seek to elucidate the physiological role of the *ana* operon to explore if and how it participates in acetogenesis and explore the dynamics of this ABC transporter that may be a hybrid between two classes of primary active transporters for Ni^{2+} acquisition.

Competing interest statement

The authors declare they have no competing financial interests.

Abbreviations

LB – Luria-Bertani, TB – terrific brother, ACN – acetonitrile, TFA – trifluoracetic acid, HEPES - (4-(2-hydroxyethyl)-1-piperazineethanesulfonic acid), IPTG – isopropyl β-D-1-thiogalactopyranosid, TCEP – tris(2-carboxyethyl)phosphine, MWCO – molecular weight cut-off, NTA – nitriloacetic acid, SDS-PAGE – sodium dodecylsulfate polyacrylamdie gel electrophoresis, TEV – tobacco endomosaic virus, FPLC – fast performance liquid chromatography, IMAC – immobilized metal-affinity chromatography, aEX – anion exchange chromatography, DETA – diethylenetriamine, EDTA -- ethylenediaminetetraacetic acid, IPFQ-LTA – intrinsic protein fluorescence quenching ligand titration assay, ICP-MS – inductively coiled plasma mass spectrometry, MALDI-ToF – matrix assisted laser desorption-ionization time-of-flight, CD – circular dichroism, PDB – Protein DataBase, IFE – Inner Filter Effect

Acknowledgements

The authors thank (1) Anna Khusnutdinova for help with experimental design and training for analytical size exclusion chromatography, and Chao Chen for data processing, (2) Dr. Bridget A. Bergquist and Joan de Vera for access to and training on their Thermo-Fisher X-Series 2 ICP-MS in the Department of Earth Sciences at the University of Toronto, and (3) Dr. Walid Houry, Vaibhav Bhandari, and Elisa Leung for access to and training on the Bruker MALDI-ToF Biotyper and the JASCO J-800 spectropolarimeter in the Department of Biochemistry at the University of Toronto. This work was supported by the Ontario Ministry of Economic Development, Job Creation and Trade through the Elements of Bio-mining ORF-RE program. PD is a recipient of an Ontario Graduate Scholarship.

References

1. Liou, J. S. C., Balkwill, D. L., Drake, G. R. & Tanner, R. S. Clostridium carboxidivorans sp. nov., a solvent-producing clostridium isolated from an agricultural settling lagoon, and reclassification of the acetogen Clostridium scatologenes strain SL1 as Clostridium drakei sp. nov. *Int. J. Syst. Evol. Microbiol.* (2005). doi:10.1099/ijs.0.63482-0
2. Cheng, C., Bao, T. & Yang, S. T. Engineering Clostridium for improved solvent production: recent progress and perspective. *Applied Microbiology and Biotechnology* (2019). doi:10.1007/s00253-019-09916-7
3. Bengelsdorf, F. R. *et al.* Bacterial Anaerobic Synthesis Gas (Syngas) and CO2 + H2 Fermentation. in *Advances in Applied Microbiology* (2018). doi:10.1016/bs.aambs.2018.01.002
4. Ragsdale, S. W. Enzymology of the Wood-Ljungdahl pathway of acetogenesis. in *Annals of the New York Academy of Sciences* (2008). doi:10.1196/annals.1419.015
5. Hood, M. I. & Skaar, E. P. Nutritional immunity: Transition metals at the pathogen-host interface. *Nature Reviews Microbiology* (2012). doi:10.1038/nrmicro2836
6. Klein, J. S. & Lewinson, O. Bacterial ATP-driven transporters of transition metals: Physiological roles, mechanisms of action, and roles in bacterial virulence. *Metallomics* (2011). doi:10.1039/c1mt00073j
7. Lewinson, O. & Livnat-Levanon, N. Mechanism of Action of ABC Importers: Conservation, Divergence, and Physiological Adaptations. *Journal of Molecular Biology* **429**, 606–619 (2017).
8. Navarro, C., Wu, L. -F & Mandrand-Berthelot, M. -A. The nik operon of Escherichia coli encodes a periplasmic binding-protein-dependent transport system for nickel. *Mol. Microbiol.* (1993). doi:10.1111/j.1365-2958.1993.tb01247.x
9. De Pina, K. *et al.* Purification and Characterization of the Periplasmic Nickel-Binding Protein NikA of Escherichia coli K12. *Eur. J. Biochem.* (1995). doi:10.1111/j.1432-1033.1995.0857p.x
10. Sebbane, F., Mandrand-Berthelot, M. A. & Simonet, M. Genes encoding specific nickel transport systems flank the chromosomal urease locus of pathogenic yersiniae. *J. Bacteriol.* (2002). doi:10.1128/JB.184.20.5706-5713.2002
11. Heddle, J., Scott, D. J., Unzai, S., Park, S. Y. & Tame, J. R. H. Crystal Structures of the Liganded and Unliganded Nickel-binding Protein NikA from Escherichia coli. *J. Biol. Chem.* (2003). doi:10.1074/jbc.M307941200
12. Cherrier, M. V. *et al.* Crystallographic and spectroscopic evidence for high affinity binding of FeEDTA(H2O)- to the periplasmic nickel transporter NikA. *J. Am. Chem. Soc.* (2005). doi:10.1021/ja0518530
13. Rowe, J. L., Starnes, G. L. & Chivers, P. T. Complex transcriptional control links NikABCDE-dependent nickel transport with hydrogenase expression in Escherichia coli. *J. Bacteriol.* (2005). doi:10.1128/JB.187.18.6317-6323.2005
14. Cherrier, M. V., Cavazza, C., Bochot, C., Lemaire, D. & Fontecilla-Camps, J. C. Structural characterization of a putative endogenous metal chelator in the periplasmic nickel transporter NikA. *Biochemistry* (2008). doi:10.1021/bi801051y
15. Cherrier, M. V. *et al.* The structure of the periplasmic nickel-binding protein NikA provides insights for artificial metalloenzyme design. *J. Biol. Inorg. Chem.* (2012). doi:10.1007/s00775-012-0899-7
16. Lebrette, H., Iannello, M., Fontecilla-Camps, J. C. & Cavazza, C. The binding mode of Ni-(L-His)2 in NikA

revealed by X-ray crystallography. *J. Inorg. Biochem.* (2013). doi:10.1016/j.jinorgbio.2012.12.010
17. Howlett, R. M., Hughes, B. M., Hitchcock, A. & Kelly, D. J. Hydrogenase activity in the foodborne pathogen Campylobacter jejuni depends upon a novel ABC-type nickel transporter (NikZYXWV) and is SlyD-independent. *Microbiol. (United Kingdom)* (2012). doi:10.1099/mic.0.054130-0
18. Lebrette, H. *et al.* Promiscuous nickel import in human pathogens: Structure, thermodynamics, and evolution of extracytoplasmic nickel-binding proteins. *Structure* (2014). doi:10.1016/j.str.2014.07.012
19. Jubier-Maurin, V. *et al.* Identification of the nik gene cluster of Brucella suis: Regulation and contribution to urease activity. *J. Bacteriol.* (2001). doi:10.1128/JB.183.2.426-434.2001
20. Lebrette, H. *et al.* Novel insights into nickel import in Staphylococcus aureus: The positive role of free histidine and structural characterization of a new thiazolidine-type nickel chelator. *Metallomics* (2015). doi:10.1039/c4mt00295d
21. Benoit, S. L., Seshadri, S., Lamichhane-Khadka, R. & Maier, R. J. Helicobacter hepaticus NikR controls urease and hydrogenase activities via the NikABDE and HH0418 putative nickel import proteins. *Microbiol. (United Kingdom)* (2013). doi:10.1099/mic.0.062976-0
22. Shaik, M. M., Cendron, L., Salamina, M., Ruzzene, M. & Zanotti, G. Helicobacter pylori periplasmic receptor CeuE (HP1561) modulates its nickel affinity via organic metallophores. *Mol. Microbiol.* (2014). doi:10.1111/mmi.12487
23. Park, K. S. *et al.* Genetic characterization of DNA region containing the trh and ure genes of Vibrio parahaemolyticus. *Infect. Immun.* (2000). doi:10.1128/IAI.68.10.5742-5748.2000
24. Hughes, A., Wilson, S., Dodson, E. J., Turkenburg, J. P. & Wilkinson, A. J. Crystal structure of the putative peptide-binding protein AppA from Clostridium difficile. *Acta Crystallogr. Sect. F* **75**, 246–253 (2019).
25. Solovyev, V. & Salamov, A. Automatic Annotation of Microbial Genomes and Metagenomic Sequences. in *Metagenomics and its Applications in Agriculture, Biomedicine and Environmental Studies* (2011).
26. Salis, H. M. The ribosome binding site calculator. in *Methods in Enzymology* (2011). doi:10.1016/B978-0-12-385120-8.00002-4
27. Mukherjee, S. & Sengupta, S. Riboswitch Scanner: An efficient pHMM-based web-server to detect riboswitches in genomic sequences. *Bioinformatics* (2016). doi:10.1093/bioinformatics/btv640
28. Edgar, R. C. MUSCLE: Multiple sequence alignment with high accuracy and high throughput. *Nucleic Acids Res.* (2004). doi:10.1093/nar/gkh340
29. Waterhouse, A. *et al.* SWISS-MODEL: Homology modelling of protein structures and complexes. *Nucleic Acids Res.* (2018). doi:10.1093/nar/gky427
30. Almagro Armenteros, J. J. *et al.* SignalP 5.0 improves signal peptide predictions using deep neural networks. *Nat. Biotechnol.* (2019). doi:10.1038/s41587-019-0036-z
31. Wiedemann, C., Bellstedt, P. & Görlach, M. CAPITO - A web server-based analysis and plotting tool for circular dichroism data. *Bioinformatics* (2013). doi:10.1093/bioinformatics/btt278
32. Biasini, M. *et al.* SWISS-MODEL: Modelling protein tertiary and quaternary structure using evolutionary information. *Nucleic Acids Res.* (2014). doi:10.1093/nar/gku340
33. Benkert, P., Biasini, M. & Schwede, T. Toward the estimation of the absolute quality of individual protein structure models. *Bioinformatics* (2011). doi:10.1093/bioinformatics/btq662
34. Gräslund, S. *et al.* Protein production and purification. *Nature Methods* (2008). doi:10.1038/nmeth.f.202
35. Andersen, K. R., Leksa, N. C. & Schwartz, T. U. Optimized E. coli expression strain LOBSTR eliminates common contaminants from His-tag purification. *Proteins Struct. Funct. Bioinforma.* (2013). doi:10.1002/prot.24364
36. Handing, K. B. *et al.* Characterizing metal-binding sites in proteins with X-ray crystallography. *Nat. Protoc.* (2018). doi:10.1038/nprot.2018.018
37. Bodenreider, C. *et al.* A fluorescence quenching assay to discriminate between specific and nonspecific inhibitors of dengue virus protease. *Anal. Biochem.* (2009). doi:10.1016/j.ab.2009.08.013
38. Tsuganezawa, K. *et al.* A fluorescent-based high-throughput screening assay for small molecules that inhibit the interaction of MdmX with p53. *J. Biomol. Screen.* (2013). doi:10.1177/1087057112460729
39. Hulme, E. C. & Trevethick, M. A. Ligand binding assays at equilibrium: Validation and interpretation. *British Journal of Pharmacology* (2010). doi:10.1111/j.1476-5381.2009.00604.x
40. Van De Weert, M. & Stella, L. Fluorescence quenching and ligand binding: A critical discussion of a popular methodology. *J. Mol. Struct.* (2011). doi:10.1016/j.molstruc.2011.05.023

41. Barber-Zucker, S., Shaanan, B. & Zarivach, R. Transition metal binding selectivity in proteins and its correlation with the phylogenomic classification of the cation diffusion facilitator protein family. *Sci. Rep.* (2017). doi:10.1038/s41598-017-16777-5
42. Dudev, T. & Lim, C. Competition among metal ions for protein binding sites: Determinants of metal ion selectivity in proteins. *Chemical Reviews* (2014). doi:10.1021/cr4004665
43. Sóvágó, I., Várnagy, K., Lihi, N. & Grenács, Á. Coordinating properties of peptides containing histidyl residues. *Coordination Chemistry Reviews* (2016). doi:10.1016/j.ccr.2016.04.015
44. Martin, R. B. A stability ruler for metal ion complexes. *Journal of Chemical Education* (1987). doi:10.1021/ed064p402
45. Dudev, T. & Lim, C. Tetrahedral vs octahedral zinc complexes with ligands of biological interest: A DFT/CDM study. *J. Am. Chem. Soc.* (2000). doi:10.1021/ja0010296
46. Irving, H. & Williams, R. J. P. 637. The stability of transition-metal complexes. *J. Chem. Soc.* (2004). doi:10.1039/jr9530003192
47. Foster, A. W., Osman, D. & Robinson, N. J. Metal preferences and metallation. *Journal of Biological Chemistry* (2014). doi:10.1074/jbc.R114.588145
48. Miethke, M. & Marahiel, M. A. Siderophore-Based Iron Acquisition and Pathogen Control. *Microbiol. Mol. Biol. Rev.* (2007). doi:10.1128/mmbr.00012-07
49. Ellermann, M. & Arthur, J. C. Siderophore-mediated iron acquisition and modulation of host-bacterial interactions. *Free Radical Biology and Medicine* (2017). doi:10.1016/j.freeradbiomed.2016.10.489
50. Arthur E. Martell and Robert M. Smith. *Critical stability constants*. (Plenum Press, 1974).

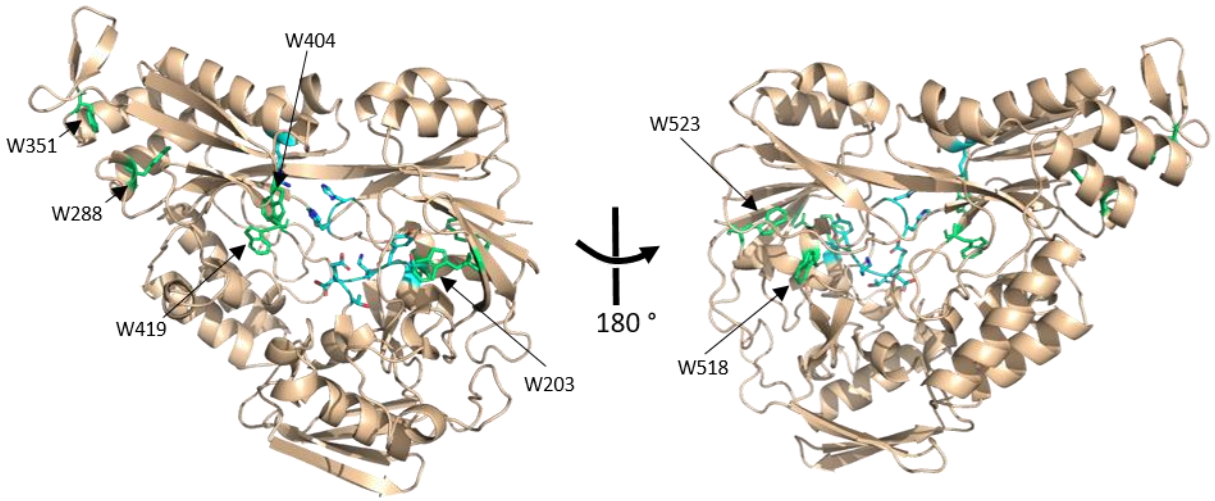

Supplementary Figure 1. Distribution of tryptophans in SBP II. Cyan residues highlight the first-shell of the binding pocket, and lime-green residues depict tryptophans. W404 and W419 are located adjacent to the binding site. W288 and W351 are located in the Western lobe. W203, W518, and W523 are located in the Eastern lobe.

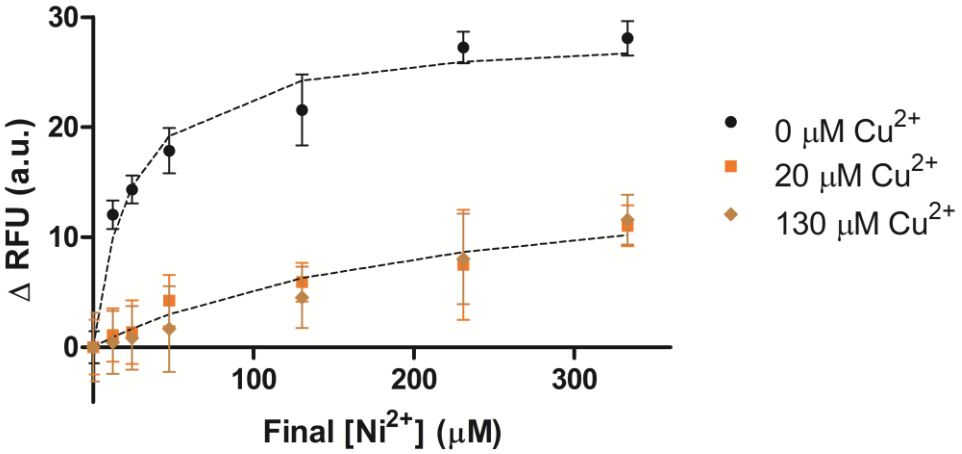

Supplementary Figure 2. Binding between nickel and *Cc*SBPII in the presence of competitor ion copper. 3 µL of *Cc*SBPII was combined with 4 µL (20 µM Cu^{2+}) or 30 µL (130 µM Cu^{2+}), and activity buffer (10 mM HEPES pH 7.2) to a final volume of 200 µL before titrating with Ni^{2}.